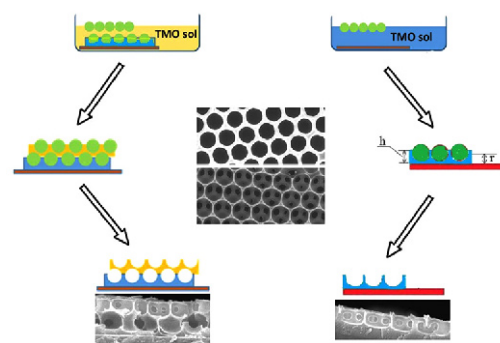


New One Step Self-assembly Strategy of Large-Area Highly Ordered, Crack-Free 2D Inverse Opal Films of Transition Metal Oxides and Its Application to Fabrication of Bilayer Inverse Opal Films

Hua Li^{*1}Jian-feng Wang¹Jacques Robichaud²Yahia Djaoued^{1*,2}¹ Department of Inorganic Materials, College of Chemistry Chemical Engineering and Materials Science, Soochow University, 199 Renai Road, Suzhou 215123, Jiangsu Province, P. R. China² Laboratoire de Recherche en Matériaux et Micro-spectroscopies Raman et FTIR, Université de Moncton-Campus de Shippagan, Shippagan, NB, E8S1P6, Canada

Received February 21, 2019 / Revised May 16, 2019 / Accepted May 19, 2019

Abstract: A new one step method for self-assembly of sacrificial polystyrene (PS) spheres colloidal crystal with a transition metal oxide (TMO) precursor matrix material is developed to fabricate highly ordered, crack-free two-dimensional (2D) TiO₂ and 2D WO₃ inverse opal (IO) films over a centimeter scale. Opal composite monolayer PS/WO₃ and PS/TiO₂ films have been successfully generated *via* simultaneous assembly of polymeric colloidal spheres floating on aqueous TiO₂ and WO₃ precursor solutions, thereby avoiding the infiltration step of the TMO precursor solution into a preassembled opal template. Large-area crack-free 2D WO₃ and 2D TiO₂ IO films were subsequently obtained after the removal of the PS opal template by chemical method. Such new strategy avoids the need for liquid infiltration into a preassembled PS opal template and minimizes the associated large cracks and inhomogeneity that often occur during the fabrication of IO films. The obtained PS/WO₃ and PS/TiO₂ opal composite monolayer films were also used as building blocks for the fabrication of highly ordered bilayer (3D) IO films with homo- and hetero-structure *via* a bottom-up, layer by layer route, through repeated operations of this new one step self-assembly method. Hence, four types of bilayer IO films were synthesized: homo-structural TiO₂ and WO₃, hetero-structural TiO₂ (bottom layer)/WO₃ (top layer) and WO₃ (bottom layer)/TiO₂ (top layer). The underlying mechanism of multilayer assembly that may account for the formation of large area crack-free multilayer films, is discussed. The electrochromic behavior of these 2D and 3D IO samples was investigated.



Keywords: one step self-assembly, inverse opal, monolayer, bilayer, TiO₂, WO₃.

1. Introduction

In the past decade, inverse opals (IOs) with two-dimensional (2D) or three-dimensional (3D) ordered structures of transition metal oxides (TMOs) have received a great deal of attention because of their practical applications in a wide range of fields, such as photonics, photocatalysis, catalysis, chromogenic devices, sensors, *etc.*¹⁻⁵ Through the works of Armstrong and Halaoui, for example, it can be established that the macroporosity of an IO film improves the performance of metal oxide thin film based devices.¹⁶ Efficiencies could be further improved if technical difficulties related to the fabrication of IO materials with uniform thickness and large area could be overcome.

Throughout the literature, various types of IOs were explored, generating a wealth of different assembly techniques. However,

Acknowledgments: The financial support of National Natural Science Foundation of China (grant #21301123), the National Science and Engineering Research Council (NSERC) of Canada ((grant #2017-05094), the John R. Evans Leaders Fund (Canada Foundation for Innovation) (grant #27741), and of the Research Assistantships Initiative of New Brunswick Innovation Fund (NBIF) is gratefully acknowledged.

***Corresponding Authors:** Hua Li (lihua123@suda.edu.cn), Yahia Djaoued (yahia.djaoued@umoncton.ca)

the synthesis of most IOs involves three sequential steps:^{7,8} (1) Self-assembly of a colloidal crystal opal template on a substrate; (2) the infiltration of a TMO precursor within the synthetic opal template, mainly by capillary action, in the form of fluid (liquid or vapour);^{9,10} (3) removal of the opal template to yield an IO by calcination, chemical etching or solvent extraction. Under such process, both the drying after self-assembly of the colloidal crystal opal template and the infiltration usually lead to cracks from uneven shrinkage, which consequently result in the unavailability of large scale IOs (<10 μm), thus limiting their applications.^{9,11,12} The infiltration techniques for IO formation, such as impregnation,¹³ dip-coating,¹⁴ interfacial materials deposition,¹⁵ and electrodeposition,¹⁶ include non-reactive and reactive routes whichever mostly, make use of capillary forces and consequently enlarge the interstices among the opal template's spheres. In such infiltration route, the colloidal crystal opal template (PS, PMMA, SiO₂ spheres) is deposited on a substrate to form a "static hard template". Once a TMO precursor is infiltrated into the colloidal crystal opal template, large cracks occur at weak connecting regions in the film, partly due to the interaction between the substrate and the colloidal crystal opal template as well as the high surface tension of the inorganic precursor aqueous solution. Efforts have been made to reduce/inhibit cracks through the

preparation of 2D colloidal crystal opal template by the floating route rendering well-ordered monolayer opal composites as starting point for infiltration of an organic precursor. For instance, Zhang and co-workers have reported a process in which they first obtained a self-assembled monolayer PS colloidal crystal opal template over deionized water deposited on a glass substrate.⁴ After the evaporation of the deionized water, the obtained PS colloidal crystal opal template was transferred to the surface of water contained in a beaker. It was then picked up with an ITO substrate and then dried at 110 °C. Then it was irradiated in an ultraviolet ozone cleaner after which a tungsten oxide (WO₃) precursor sol was drop-casted over the PS colloidal crystal opal template, resulting in a PS/WO₃ opal composite monolayer. After drying and annealing, a WO₃ IO film was obtained.

Recently, our group developed an alternative route, in which a limited number of steps were used, allowing the formation of large area morphology-controlled 2D PS/TMO opal composite films directly on ITO substrates. It also avoids the possible formation of cracks during the infiltration step. Indeed, contrary to the above described strategy where infiltration is done into a static PS hard opal template, in our strategy, during the infiltration step, the PS spheres can move to accommodate the TMO sol. We called this route “dynamic hard-template infiltration strategy”. First, a PS colloidal crystal opal template is directly self-assembled at the air/water interface and then, a TMO precursor solution is injected underneath the floating colloidal PS opal film. Driven by the capillary action, the TMO will penetrate the interstitial spaces between the free moving PS spheres from underneath, resulting in a floating PS/TMO opal composite film. Once an ITO substrate is placed under the PS/TMO opal composite monolayer, the solution is slowly sucked out to deposit the PS/TMO opal composite onto the ITO substrate. After the removal of the PS spheres, 2D large area crack-free TMO IO on ITO substrates are obtained.⁵

In this work, we improved the strategy and developed a new simple, fast one step route for the fabrication of large-area crack-free 2D PS/TMO opal composite monolayers on ITO substrates. Instead of using water as the floating medium for the self-assembly of the 2D PS spheres colloidal crystal opal template, as it was done in the original “dynamic hard-template infiltration strategy”, a TMO precursor solution is used. Then, 2D PS spheres colloidal crystal opal films are self-assembled at the air/liquid interface by floating on the surface of the TMO precursor solution, yielding a PS/TMO opal composite monolayer film in a single step, thereby avoiding the infiltration step of the TMO precursor solution into a preassembled opal template. Large-area crack-free 2D TMO (WO₃ or TiO₂) IO films are subsequently obtained after the removal of the PS opal template by chemical method. We also show that the 2D PS/TMO opal composite monolayers can be used as building blocks for the fabrication of highly ordered multilayer (3D) TMO IO films with homo- or hetero-structure in a bottom-up approach through a layer by layer route *via* repeated operations of this new strategy.

2. Experimental

2.1. Material

The non-cross linked monodispersed carboxyl polystyrene parti-

cles (530 nm in diameter) in aqueous suspension (5.0%w/v) were purchased from Spherotech Inc. Before using, they were further diluted using various volume ratio of water to ethanol. ITO slides were sonicated successively in warm water, acetone, ethanol and deionized water for 15 min, respectively. Tungsten powder (12 μm, 99.9%) was purchased from Aldrich. Ammonium hydroxide (25%~28%), H₂O₂ (30%), titanil sulfate (TiO-SO₄·nH₂O, 99%) and H₂SO₄ (98%) were purchased from Sinopharm Group Co. Ltd. Analytically pure tetrahydrofuran (THF), sodium dodecylsulfate (SDS) and Millipore water were purchased from J&K Scientific and used as received without further purification. All the aqueous solutions were prepared with Millipore water (resistance=18.2 MΩ cm⁻¹).

2.2. Synthesis of WO₃-precursor solution

A WO₃ solution was made by dissolving 0.21 g of tungsten powder in 2.2 mL H₂O₂ (30 %). After the initial reaction for 20 minutes in an ice-bath, the mixture was left to stir at room temperature for 18 h to get a clear solution, and then refluxed at 100 °C for 1 h to get a transparent orange solution. Then, the solution was diluted with 6.8 mL water.

2.3. Synthesis of TiO₂-precursor (peroxotitanium acid (PTA)) sol

Tetanyl sulfate (0.70 mL) was first dissolved in 27 mL water and 7.2 mL of ammonia aqueous solution (3 mol/L) was added, resulting in a white precipitate. The precipitate was washed with water to remove the NH₄⁺ and SO₄²⁻ impurity ions and then peptized in a mixed solution of 10 mL water and 5 mL H₂O₂ (30%) for 20 h in an ice bath, under continuous slow stirring, to get a transparent orange-red TiO₂-precursor sol.^{17,18}

2.4. Fabrication of PS/WO₃ and 2D PS/TiO₂ opal composite monolayers, WO₃ and TiO₂ IO monolayer, homo-structural TiO₂ and WO₃, hetero-structural TiO₂/WO₃ and WO₃/TiO₂ bilayer IO films

A clean ITO glass slide was placed on the bottom of a Petri dish (Ø=9 cm). Then, a TMO (WO₃ or TiO₂) sol was added to submerge the ITO glass slide. Next, diluted PS particles suspension was added drop-by-drop into the WO₃ (or PTA) solution in the Petri dish. Then, one or two drops of 2 wt.% sodium dodecylsulfate solution were added into the TMO sol from a corner of the dish. After 20 min, a close-packed 2D PS/WO₃ (or PS/TiO₂) opal composite monolayer was self-assembled on the surface of the TMO sol. Next, the solution was slowly sucked out to sink the opal composite monolayer film onto the ITO substrate. After drying in air (for PS/TiO₂, drying under ice-bath is also needed), the 2D PS/WO₃ (or PS/TiO₂) opal composite monolayer was further dried in an oven at 65 °C for 2 h. Thus, 2D PS/WO₃ and 2D PS/TiO₂ opal composite monolayer films were obtained, namely PW-m65 and PT-m65, in which P, W, T, m, 65 refer to PS template, WO₃, TiO₂, monolayer and 65 °C, respectively.

To remove the PS spheres and get 2D WO₃ and TiO₂ IO films, PW-m65 and PT-m65 were treated in THF for 2h, followed by

heat treatment under 150 °C for 2h to allow the IO films to dry and stick well to the ITO substrate. The resulting 2D IO films were named W-m150 and T-m150 in which W, T, m, and 150, refer to WO_3 , TiO_2 , monolayer, and 150 °C, respectively. TiO_2 2D IO (T-m300) monolayer films were further obtained by heat treatment of 2D T-m150 under 300 °C for 2 h.

Following the same sequence as for the fabrication of PT-m65 and PW-m65, PS/ TiO_2 and PS/ WO_3 homo-structural opal composite bilayer films were obtained by replacing the bare ITO substrates with previously formed PT-m65 and PW-m65. The resulting PS/ TiO_2 and PS/ WO_3 opal composite homo-structural bilayer films were named PT-b65 and PW-b65, in which P, T, W, b, 65 refer to PS template, TiO_2 , WO_3 , bilayer and 65 °C, respectively. Further removal of the PS spheres and proper heat treatment as described before gave place to TiO_2 and WO_3 homo-structural bilayer IO films, named as T-b300 and W-b150, respectively.

Similarly, PS/ TiO_2 (bottom layer)/ WO_3 (top layer) and PS/ WO_3 (bottom layer)/ TiO_2 (top layer) opal composite hetero-structural bilayer films were obtained and named as PWT-b65 and PTW-b65, respectively. Further removal of the PS spheres and proper heat treatment as described before gave place to TiO_2 / WO_3 and WO_3 / TiO_2 hetero-structural bilayer IO films, named as TW-b300 and WT-b300, respectively.

2.5. Electrochromic properties of the fabricated IO samples

The electrochromic (EC) behavior of obtained WO_3 and TiO_2 monolayer IOs, WO_3 and TiO_2 homo-structural bilayer IOs, TiO_2 / WO_3 and WO_3 / TiO_2 hetero-structural bilayer IOs were conducted with ECDs Cyclic Testing System (Zhuhai Kaivo Optoelectronic Technology Co., Ltd.) in which the working electrode consisted of EC materials (IOs) deposited on the ITO substrate. The counter electrode was a platinum grid (25×25 mm, 52 mesh, 0.1 mm in diameter). All these measurements were performed in 0.1 mol/L sulphuric acid (H_2SO_4) as the electrolyte.

2.6. Characterization

Morphologies of the films were characterized using a field-emission scanning electron microscope (SEM, Hitachi S-570). The optical transmittance spectra of the films and of the devices in their colored states were obtained using a PERSEETU-1810PC UV-vis-NIR spectrophotometer. An ALRS-5 Micro-Raman Spectrometer was used to record the Raman Spectra at room temperature. Powder XRD patterns were recorded by using a Rigaku D/Max2200PC diffractometer with Cu Ka radiation (40 kV and 40 mA) with a scanning rate of 10°min^{-1} .

To test the content of W and Ti in TW-b300, further energy dispersive X-ray spectroscopy (EDS) analysis was conducted by EDS through testing the powder of films peeled off the ITO substrates.

3. Results and discussion

3.1. One step assembly of large-area crack-free 2D WO_3 or TiO_2 IO monolayer films

In this work, the large-area highly ordered, crack-free 2D inverse

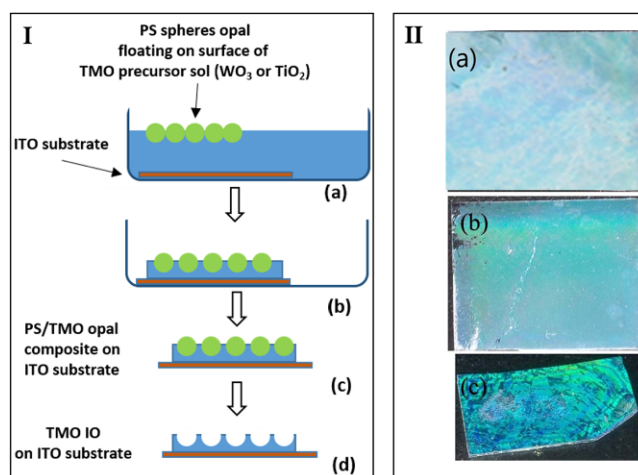


Figure 1. (I) Schematic illustration of the fabrication process of large-area, crack-free 2D inverse opal monolayer films of WO_3 and TiO_2 . (II) Optical photographs of the PS/ TiO_2 opal composite monolayer films on various substrates: (a) Soda lime substrate (20 mm×25 mm); (b) ITO coated-glass substrate (20 mm×25 mm); (c) silicon substrate (10 mm×20 mm).

opal (IO) monolayer films of WO_3 and TiO_2 were fabricated through the process illustrated in Figure 1(I)((a) to (d)). Firstly, a clean ITO glass slide was placed on the bottom of a Petri dish, and a WO_3 (or TiO_2) precursor sol is added to submerge the slide. Then, an aqueous-alcoholic colloidal suspension of PS spheres (530 nm in diameter) was spread on the surface of the WO_3 (or TiO_2) precursor sol. The interaction forces among the spheres resulted in a well-ordered opal monolayer over a large area at the air- WO_3 (or TiO_2) precursor sol interface. Simultaneously, while the PS spheres self-assembled into a well-ordered periodic opal template, the precursor sol infiltrated the interstices of the colloidal spheres to form a PS/ WO_3 (or PS/ TiO_2) opal composite monolayer structure floating over the corresponding precursor sol (Figure 1(I)(a)). Next, the sol contained in the system was slowly sucked out in order to have the opal composite monolayer deposit onto the ITO substrate (Figure 1(I)(b)). After drying, a PS/ WO_3 (PW-m65) and PS/ TiO_2 (PT-m65) opal composite monolayer films on ITO substrate were obtained (Figure 1(I)(c)).

There are several advantages for this technique. First, this process avoids the infiltration step of the TMO precursor solution into a preassembled opal template. Second, it takes only half an hour to obtain large-area crack-free PS/TMO opal composite monolayer films. Finally, the PS/TMO opal composite films can be deposited on any kind of substrates regardless of surface wettability and smoothness. Figure 1(II) shows typical optical photographs of a PS/ TiO_2 opal composite monolayer (PT-m65) deposited on three kinds of substrates regardless of their hydrophilic or hydrophobic properties such as soda lime glass (Figure 1(II)(a)), ITO (Figure 1(II)(b)) and silicon (Figure 1(II)(c)).

WO_3 and TiO_2 IO monolayer films (Figure 1(I)(d)) were produced after removal of the PS opal template from the PW-m65 and PT-m65 opal composite monolayer films by THF and applying proper heat treatment after step I(c) as described in the experimental section. The obtained WO_3 and TiO_2 IO monolayer

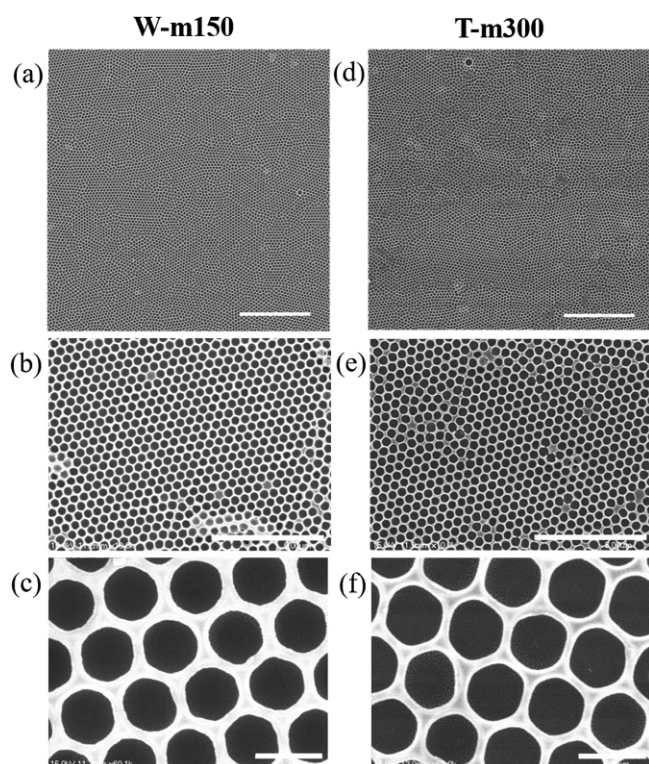


Figure 2. Different magnifications SEM images of W-m150 (a) to (c) and T-m300 (d) to (f) showing crack-free samples. Scale bars: (a) and (d) 10 μm ; (b) and (e) 5 μm ; (c) and (f) 0.5 μm .

films were named W-m150 and T-m300, respectively. The SEM images of Figure 2(a) to (f) show well-ordered monolayer films obtained after the removal of the PS opal templates from the opal composites monolayer films. Figure 2(a) and (d), present typical low magnification SEM images of W-m150 and T-m300 respectively, revealing large area crack-free IO films. The magnified SEM images (Figure 2(b), (c), (e), and (f)) of the films display the formation of honeycomb structures with hexagonal symmetry.

3.2. Optimisation of the aqueous-alcoholic PS colloidal suspension

During the experiments, it was established that the volume ratio of water to ethanol in the PS spheres suspension plays a key role in obtaining a well-ordered IO monolayer film. Figure 3 shows the SEM images of typical W-m150 monolayer samples, synthesized by using various ratio of water to ethanol in the PS colloidal suspension. When a PS spheres colloidal solution of 0.5 wt.% with a 1:1 water to ethanol ratio is used, the PS spheres show viscous diffusion and accordingly, only small fragments of PS opals are formed. Afterwards, under the surface tension from sodium dodecylsulfate (SDS), these fragments contact with each other to form larger fragments which, due to limited movement, have difficulty to reunite into a large well oriented opal area. At the end of the fabrication process, the obtained IO monolayer film present many anomalous areas (Figure 3(a)). Fortunately, the orientation improves with an increasing ratio of water to ethanol. When the ratio reached

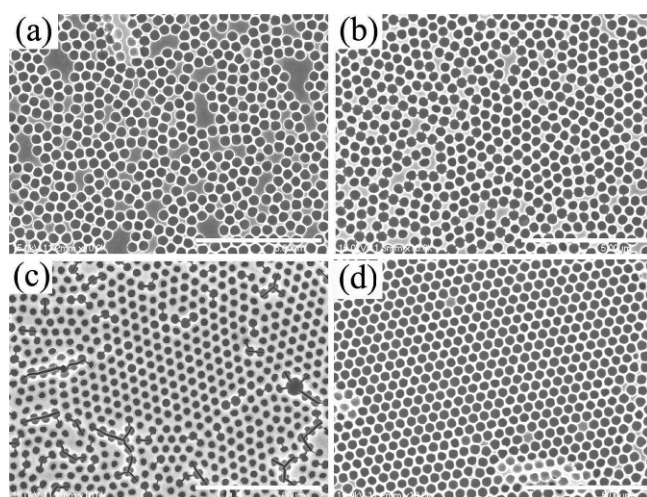


Figure 3. SEM images of typical W-m150 monolayer samples obtained by using various ratio of water to ethanol in PS colloidal suspension. (a) 1:1, 0.5 wt.%; (b) 1.5:1, 0.5 wt.%; (c) 2:1, 0.5 wt.%; (d) 2:1, 0.35 wt.%. Scale bars: 5 μm .

2:1, the array of PS spheres is greatly improved. Also, once the array becomes well ordered, the corresponding infiltration of the TMO liquid matrix sol is increased as shown in Figure 3(c), in which a thicker framework is observed. Such phenomenon could be attributed to higher capillary forces. Based on such observation, the lowering of the PS suspension concentration to 0.35 wt.% while keeping the same water to ethanol ratio of 2:1 resulted in a much-improved array IO monolayer film as shown in Figure 3(d). Good results cannot be obtained when the water to ethanol ratio is higher than 2:1 since the PS spheres sink into the liquid matrix sol.

3.3. Fabrication of TiO_2 or WO_3 homo-structural bilayer IO films, and WO_3/TiO_2 or TiO_2/WO_3 hetero-structural bilayer IO films

After the successful fabrication of 2D WO_3 and TiO_2 IO monolayer films, the fabrication of TiO_2 and WO_3 homo-structural bilayer IO films (respectively denoted as T-b300 and W-b150), as well as WO_3 (bottom layer)/ TiO_2 (top layer) and TiO_2 (bottom layer)/ WO_3 (top layer) hetero-structural bilayer IO films (respectively denoted as WT-b300 and TW-b300) was also attempted through a layer by layer route. The preparation of the TMO homo- or hetero-structural bilayer IO films by this approach is illustrated in Figure 4. For the formation of WO_3 or TiO_2 homo-structural bilayer IO films, differently from literature⁴ in which a WO_3 IO film was directly used as substrate for the deposition of a second layer, here, a PS/ WO_3 or a PS/ TiO_2 opal composite monolayer film (Figure 4(a)) was used as bottom layer which served as support upon which another PS/ WO_3 or PS/ TiO_2 opal composite monolayer was added, rendering possible the formation of PS/ TiO_2 (PT-b65) and PS/ WO_3 (PW-b65) homo-structural opal composite bilayer films (Figure 4(b)). After removal of the PS spheres template, and proper heat-treatment, large area WO_3 (W-b150) and TiO_2 (T-b300) homo-structural bilayer IO films were obtained (Figure 4(c)). Figure 5(a), (b), (d) and (e) show

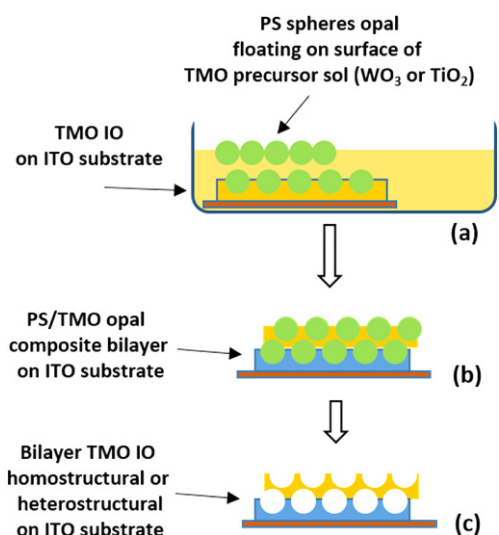


Figure 4. Schematic of the preparation of TMO homo- or hetero-structural bilayer IO films.

respectively the magnified SEM images of W-m150, W-b150, T-m300 and T-b300 IO films. The herein described route also adds versatility to the process, permitting the fabrication of

TiO₂/WO₃ or WO₃/TiO₂ hetero-structural bilayer IO films, where a PS/WO₃ opal composite monolayer is used as bottom layer on which a second PS/TiO₂ opal composite monolayer is deposited or vice-versa. The magnified SEM images of Figure 5(c) and (f) are respectively, those of WT-b300 and TW-b300 hetero-structural bilayer IO films. All of these films, templated by using 530 nm PS spheres, show honeycomb structure with circular upper-end openings. Inner pores at the bottom of the macroporous structure of the first layer in the bilayer films (Figure 5(b), (c), (e), (f)) are also apparent. This demonstrates that the porous network is interconnected throughout all bilayers, allowing a good diffusion of guest materials, which is a major advantage for many potential applications since the accessibility and diffusion of chemical species within the structure is enhanced.

Figure 6 shows cross-sectional SEM images evidencing the thicknesses of the IO films on ITO substrates: W-m150 (Figure 6(a)), W-b150 (Figure 6(b)), WT-b300 (Figure 6(c)), T-m300 (Figure 6(d)), T-b300 (Figure 5(e)) and TW-b300 (Figure 6(f)). The long-range horizontal ordering and virtual absence of defects in each layer is apparent. No collapse of the walls was found for the bottom layers, this is due to the reduction of the number of steps involved in the fabrication of IO films and the use of room temperature during the fabrication process and

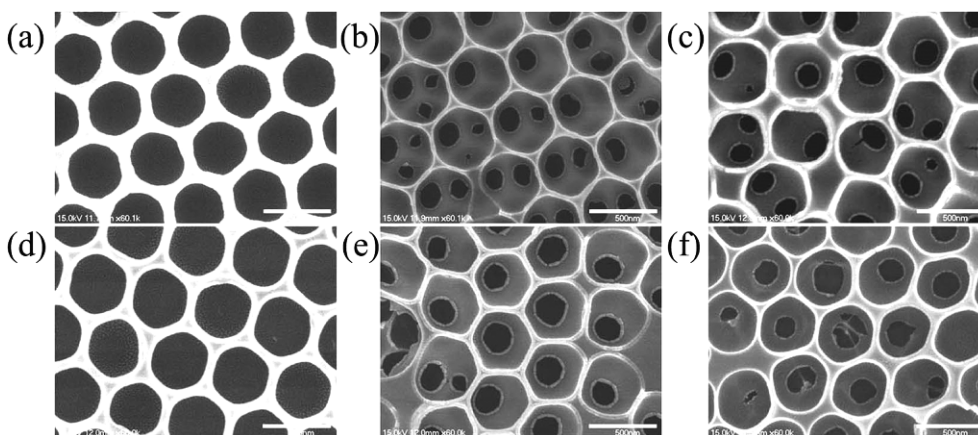


Figure 5. SEM images for samples. (a) W-m150; (b) W-b150; (c) WT-b300; (d) T-m300; (e) T-b300; (f) TW-b300; scale bars: 500 nm.

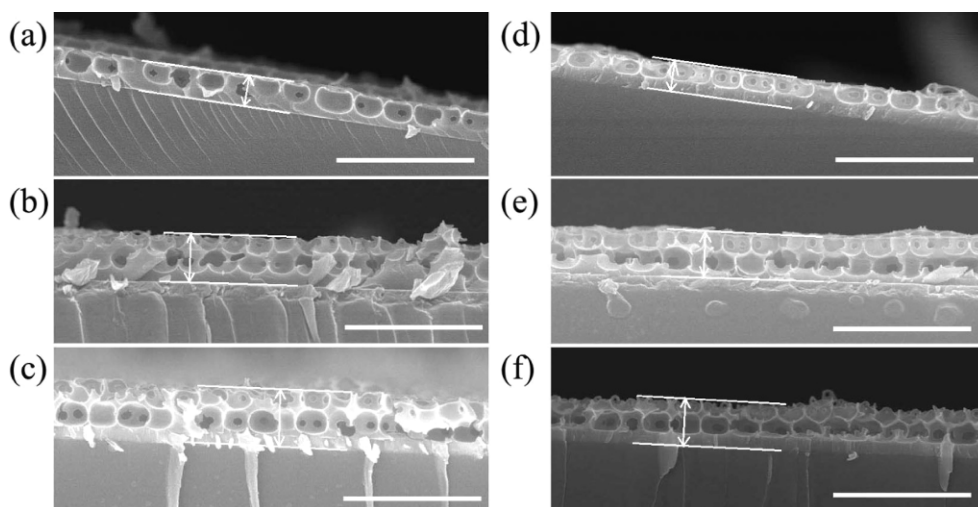


Figure 6. Cross-sectional SEM image of samples: (a) W-m150 (thickness: 450 nm); (b) W-b150 (thickness: 725 nm); (c) WT-b300 (thickness: 815 nm); (d) T-m300 (thickness: 425 nm); (e) T-b300 (thickness: 700 nm); (f) TW-b300 (thickness: 720 nm); arrows show the thickness of films to be measured, scale bars: 2 μm.

removal of the PS spheres by chemical means instead of calcination. Furthermore, the thicknesses of the films increase with the number of layers from around 400 nm for monolayer to above 700 nm for bilayer. During the infiltration of the first layer, the TMO liquid matrix sol will not wholly fill the interstitial space between the PS spheres of the opal template, but only get slightly higher than half of the diameter of the PS spheres. During the synthesis of the second layer, the TMO liquid matrix sol first infiltrates the bottom layer, which gets wholly filled and then infiltrates the top layer up to more than half the diameter of the PS spheres. Thus, it is reasonable to deduce that the thicknesses of the films are nearly proportional to the number of layers. The fabrication mechanism of bilayer IO films is treated in section 3.4.

The pore depth of WO_3 (W-m150) and TiO_2 (T-m300) monolayer IO films are respectively estimated to be 272 and 233 nm whereas the corresponding pore width are respectively 411 and 386 nm. The film thicknesses are cited in the caption to Figure 6 as well as in Table 1, along with their estimated pore depth and pore width.

3.4. Mechanism of fabrication of bilayer IO films

As for the fabrication of bilayer (and multilayer) IO films, during the formation of the second layer, the PS spheres of the PS/ WO_3 (or PS/ TiO_2) opal composite film act as support for the second layer, retaining the skeleton of the ordered array after the removal of the PS template, hence, preserving the macroporous structure throughout the bilayer IO films. However, it should be stressed here, that the filling height of the matrix in the first (or bottom) layer, used as substrate, is important to successfully overlap a second (or top) layer, as illustrated in Figure 7. When the height (h) of the matrix is less than the height of the center position (r) of the PS spheres in the opal template (Figure 7(a, 1)), the PS template easily dislocates from the matrix (Figure 7(a, 2)) after the monolayer film substrate is immersed into the aqueous matrix solution. As a result, the second (top) matrix layer would sink onto and cover the bottom matrix layer (Figure 7(a, 3)), the worst result of which would be to block the ordered pores of the bottom matrix layer. Otherwise, when the height of the matrix is higher than the center position of the PS spheres (Figure 7(b, 1)), the matrix plays a key role in 'fixing' those PS spheres by clamping them tightly to the inorganic matrix when

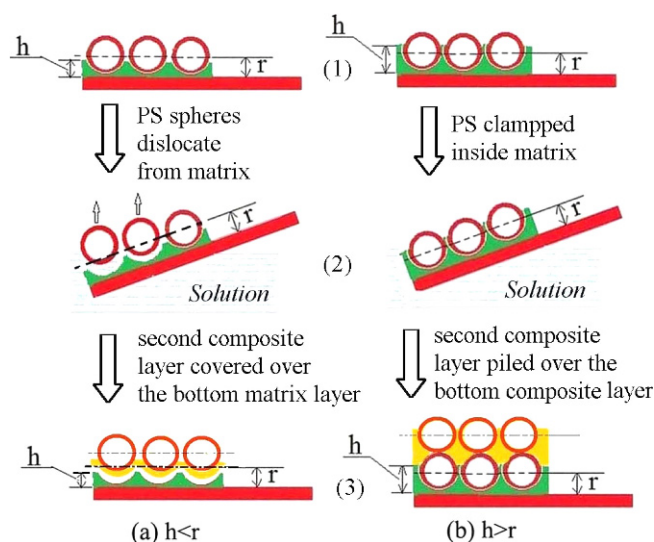


Figure 7. Two possible results when a PS/nanoparticles opal composite film substrate is inserted into the aqueous matrix solution during the synthesis of the second opal composite layer (h =height of the nanoparticle matrix framework, r =height of the radius position of the PS spheres in the opal template). (a) $h < r$: PS spheres are peeling off the nanoparticle matrix framework; (b) $h > r$: PS spheres are clamped inside the nanoparticle matrix framework.

the opal composite monolayer film used as substrate is immersed into the aqueous matrix solution (Figure 7(b, 2)). Consequently, such perfect bottom layer endows the possibility to support another composite film while avoiding the risk of the macroporous structure being blocked (Figure 7(b, 3)). Such assumption is demonstrated by cross-sectional SEM observation (Figure 8) of TiO_2 IO films. Typically, the PS spheres of the opal template are well 'trapped' by the TiO_2 precursor matrix solution with a lid-like head exposed (Figure 8(a)). The sizes of the 'lids' are less than the half diameter of the PS spheres. After the removal of the PS spheres, the depth of pores is measured to be around 322 nm (Figure 8(b)) which is more than the radius of the PS spheres (265 nm).

3.5. Raman, XRD and EDS analysis of the fabricated IO films

Figure 9(a) shows the Raman spectra of the WO_3 monolayer (W-m150), WO_3 bilayer (W-b150) and WO_3 (bottom layer)/

Table 1. Estimated IO films thicknesses and pore dimensions

Sample	Thickness (nm)	Pore width (nm)		Pore depth (nm)	
W-m150	450	411		272	
W-b150	725	1 st layer	422	1 st layer	296
		2 nd layer	359	2 nd layer	230
T-m300	425	386		233	
T-b300	700	1 st layer	415	1 st layer	309
		2 nd layer	389	2 nd layer	242
WT-b300	815	1 st layer	431	1 st layer	380
		2 nd layer	357	2 nd layer	277
TW-b300	720	1 st layer	417	1 st layer	283
		2 nd layer	379	2 nd layer	229

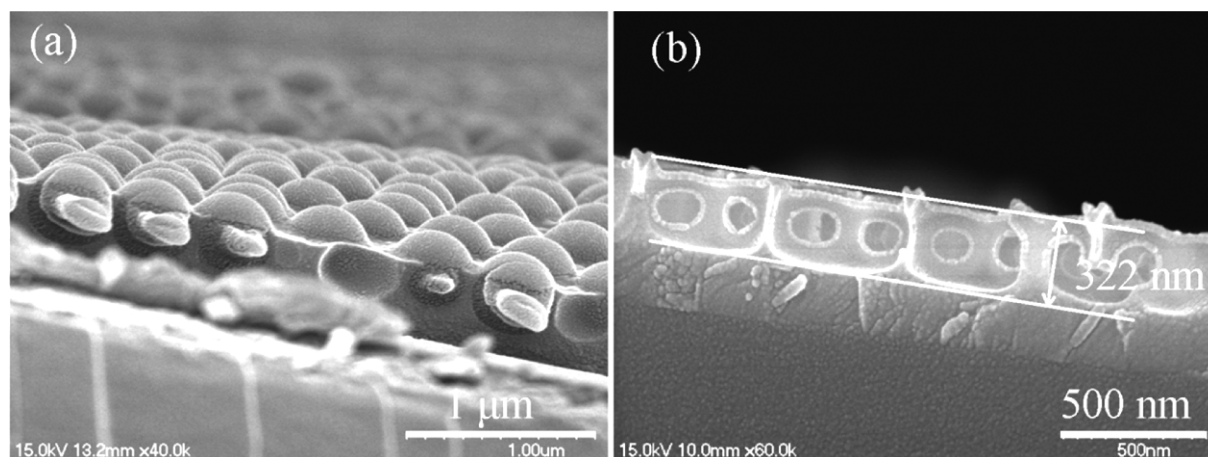


Figure 8. Cross-sectional SEM images (a) of the PS/TiO₂ opal composite monolayer film (PT-m65), (b) TiO₂ IO monolayer film (T-m300) after the removal of the PS spheres of 530 nm diameter.

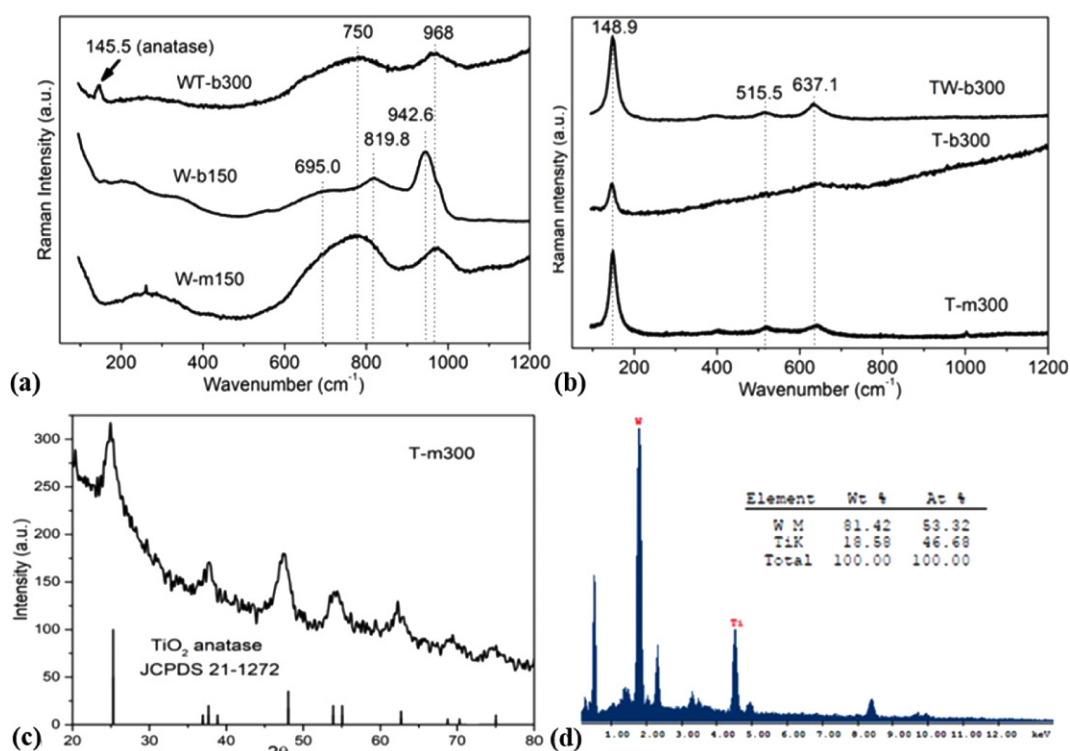


Figure 9. (a) and (b), Raman spectra of the W-series and T-series, respectively; (c) XRD of sample T-m300; (d) EDS results of TW-b300, demonstrating the existence of the WO₃ in the sample.

TiO₂ (top layer) hetero-structural bilayer (WT-b300) IO films. There are no signals from PS spheres in all the samples, demonstrating that the polymer template has been thoroughly removed. All the samples show amorphous tungsten oxide with the W=O stretching mode observed at about 968 cm⁻¹ and a broad band with a maximum at 750 cm⁻¹ for W-m150 and WT-b300. For W-b150, the W=O stretching mode is seen at around 943 cm⁻¹, along with two intensity bands at around 820 and 695 cm⁻¹. In the Raman spectrum of the WT-b300 sample, in addition to the peaks, which are characteristic features of the amorphous WO₃ IO bottom layer, the mode emerging at 145.5 cm⁻¹ is due to TiO₂ IO top layer in the anatase phase. Raman spectra of the TiO₂ monolayer (T-m300), TiO₂ bilayer (T-b300) and TiO₂ (bottom layer)/WO₃ (top layer) hetero-structural bilayer (TW-b300) IO

films are displayed in Figure 9(b). The Raman modes appearing at 148.9 (E_g), 515.5 (B_{1g}) and 637.1 cm⁻¹ (E_g) in all samples are those of anatase TiO₂.¹⁹ The main band is broadened (up to ~22 cm⁻¹) and high-frequency shifted (148.9 cm⁻¹) as compared to commercial anatase TiO₂ powder from Aldrich (142.5 cm⁻¹ with a FWHM of 7.5 cm⁻¹). Using a phonon confinement model, it was possible to estimate the crystallite size from the FWHM and the position of the anatase main Raman peak of the samples containing titania.²⁰ The evolution of crystallite size is shown in Table 2. In the T-m300, TW-b300, T-b300, and WT-b300 samples, the anatase main Raman peak is centered respectively at 149.2, 149.9, 146.5, and 145.5 cm⁻¹, with a FWHM of 20.1, 22.1, 17.6, and 14.3 cm⁻¹. Each of these samples give respectively, an average crystal size of 6.0, 5.9, 7.5, and 9.1 nm. We attributed

Table 2. TiO₂ anatase films crystallite sizes

Sample	Size from Raman data				From XRD data
	Peak position (cm ⁻¹)	Size (nm)	FWHM (cm ⁻¹)	Size (nm)	Size (nm)
T-m300	149.2	5.7	20.1	6.3	5.5
T-b300	146.4	8	17.6	6.9	
TW-b300	148.9	5.9	22.1	5.9	
WT-b300	145.5	9.3	14.3	9.0	

such large shifts and broadening of the main Raman band of the anatase phase mainly to the particle quantum size effect.²⁰ The formation of anatase nanocrystals with an average particle diameter of ~5.5 nm was also evidenced by X-ray powder diffraction (XRD) measurements for T-m300 sample (see Figure 9(c)). Further EDS analysis was conducted to test the content of W and Ti in TW-b300 sample, through testing the powder of films peeled off the ITO substrates, since the WO₃ did not show in the Raman spectrum (see Figure 9(d)).

3.6. UV-vis-NIR transmittance spectra of the fabricated IO films

Figure 10(a-c) and (d) show, respectively, the UV-vis-NIR transmittance spectra of titanium oxide inverse opal films (T-m300, T-b300 and TW-b300 IO films, denoted as T series); tungsten oxide inverse opal films (W-m150, W-b150 and WT-b300, denoted as W series); and their corresponding PS/TiO₂ opal composite films (PT-m65, PT-b65 and PTW-b65, denoted as PT series); and PS/WO₃ opal composite films (PW-m65, PW-b65, and PWT-b65,

denoted as PW series) along with their corresponding optical reflection images (see insets). All samples show mainly blue color revealing the corresponding photonic band gaps. In contrast to monolayer, all bilayer samples show a little blue shift for the absorption of light from the T-m300, W-m150 films (around 500 nm for bilayer films as compared to 530 nm for monolayers). Apart from the absorption at 500 nm, there are several minor absorptions from 500 to 600 nm, contributing to the blue color at various levels (Figure 10(a), (b)). PT and PW series show nearly similar response as their corresponding TiO₂ and WO₃ IOs with blue shifts when the layer thickness increases. Apart from that, in contrast to their IOs counterpart, the absorption of light for PT and PW composite films show some red shift around 550 nm which explains the pale pink blue observed in the optical reflection images of the opal composite samples.

3.7. Electrochromic properties of the fabricated IO films

The electrochromic behavior of the W and T series was evaluated and their optical transmittance spectra in their colored and

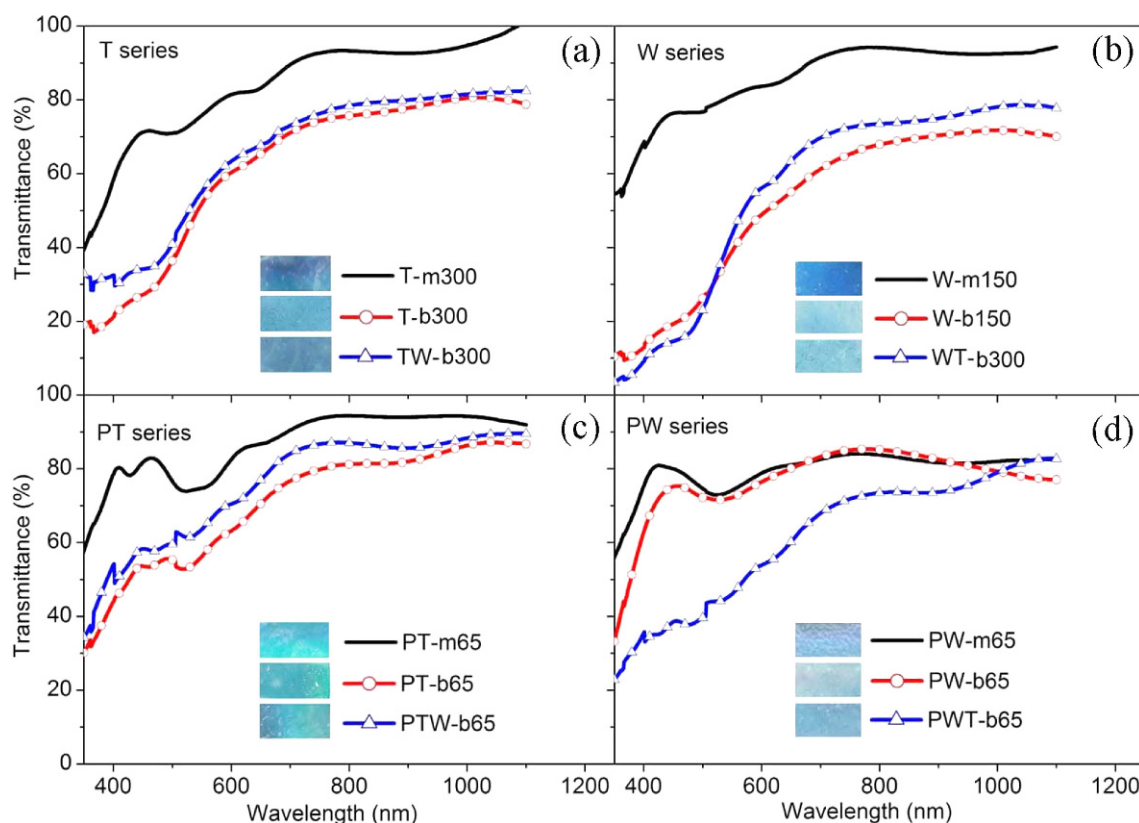


Figure 10. UV-vis-NIR transmittance spectra of T (a), W (b), PT (c), and PW (d) series. Insets show the corresponding optical reflection images of the films on black background.

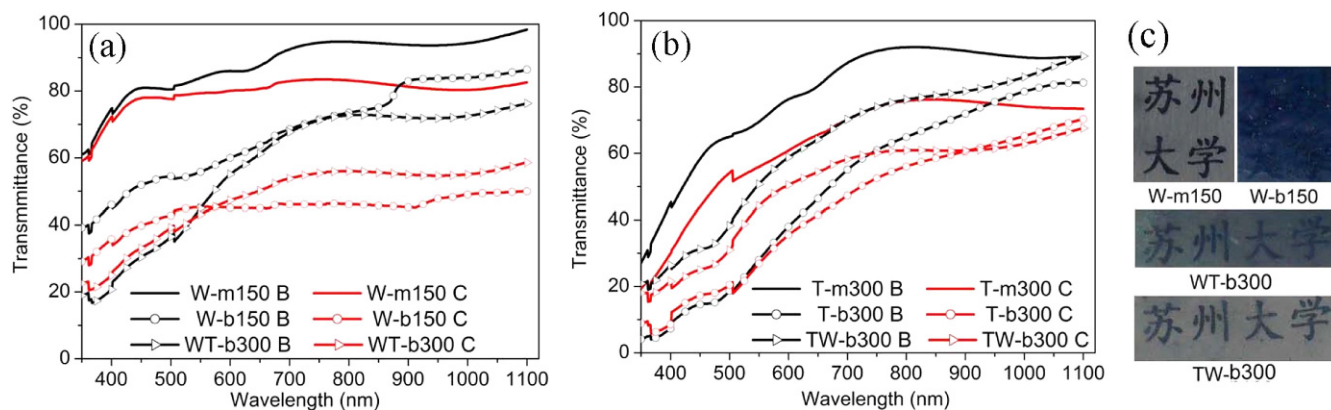


Figure 11. Transmittance spectra of WO_3 IO based films series (a) and TiO_2 IO based films series (b) recorded at colored (1.5 V, 10 s, C, red lines) and bleached (-1.5 V, 10 s, B, black lines) states: monolayer IOs (W-m150 and T-m300, solid line); bilayer IOs (W-b150 and T-b300, circles) and hetero-structural bilayer IOs (WT-b300 and TW-b300 IO, triangles). (c) typical photographs of the IO films at the colored states, illustrating a distinct optical contrast.

Table 3. Electrochromic optical modulation-cycle 1

Sample	T (%) at 700 nm		T (%) at 1100 nm		ΔT (%) at 700 nm ^a	ΔT (%) at 1100 nm ^b
	Bleached	Colored	Bleached	Colored		
W-m150	92.5	82.9	98.4	82.5	9.6	15.9
W-b150	68.6	46.0	86.4	50.0	22.5	36.4
WT-b300	67.7	53.8	76.3	58.6	13.9	17.7
T-m300	87.0	70.1	89.2	73.4	16.9	15.8
T-b300	55.1	48.5	81.3	70.3	6.6	11
TW-b300	70.2	57.8	89.3	77.6	12	21.7

^a ΔT (%) at 700 nm = $T\%$ at 0 V - $T\%$ at 700 nm 1.5 V. ^b ΔT (%) at 1100 nm = $T\%$ at 0 V - $T\%$ at 1.5 V.

bleached states for applied potential of ± 1.5 V are respectively presented in Figure 11(a) and (b). The actual photographs of the W-m150, W-b150, WT-b300 and TW-b300 IO films in their colored states are also presented in Figure 11(c).

In the bleached state, the transmittance of the films at a wavelength of 700 nm (Vis) was 92.5% for W-m150, 68.6% for W-b150, and 67.7% for WT-b300, whereas, at a wavelength of 1100 nm (NIR), the transmittance was 98.4% for W-m150, 86.4% for W-b150, and 76.3% for WT-b300 as shown in Table 3. When a coloration potential of 1.5 V was applied, the transmittance of the films at a wavelength of 700 nm exhibited an optical contrast of 9.6%, 22.5%, and 13.9% for W-m150, W-b150, and WT-b300, respectively. At a wavelength of 1100 nm the corresponding exhibited values of optical contrasts were 15.9%, 36.4%, and 17.7%. For the WO_3 IO films, a large increase of the optical contrast is observed between the monolayer and bilayer films. However, one can see that TiO_2 contributes little to the optical contrast of the hetero-structural bilayer WT-b300, which is 13.9%, while it is 22.5% for the homogenous bilayer W-b300. An optical contrast of 12% at a wavelength of 700 nm, is exhibited by the hetero-structural bilayer TW-b300 which is nearly the same as that of hetero-structural bilayer WT-b300. Obviously, under the present experiment, the cooperative contribution of TiO_2 and WO_3 to each other for the optical contrast is minor, partly due to their limited contact surface area.

4. Conclusions

In summary, highly ordered, crack free monolayer and bilayer TiO_2 and WO_3 inverse opal films were synthesized by a novel one step self-assembly route. Concurrently, monolayer composite colloidal crystal films consisting of polymeric colloidal spheres floating on an aqueous TiO_2 - (or WO_3 -) precursor solution were successfully prepared. In this method, instead of using water as the floating medium for the self-assembly of the 2D PS spheres colloidal crystal opal template, like it was done in the conventional process, a TMO precursor solution is used, yielding a PS/TMO opal composite monolayer film after only one step, thereby avoiding the infiltration step of the TMO precursor solution into a preassembled opal template. Such novel route was further used to fabricate bilayer TiO_2 or WO_3 homo-structural, and TiO_2/WO_3 or WO_3/TiO_2 hetero-structural bilayer films through a layer by layer route *via* repeated operations of this new one step self-assembly method. The underlying mechanism for multilayer assembly is discussed, bringing in evidence that the thickness of the inorganic matrix plays an important role in 'clamping' of the templates to prevent peeling of the PS template when the monolayer PS/inorganic matrix is used as bottom framework. Due to the highly ordered macroporous texture, allowing an improved access to the electrolyte, the WO_3 monolayer and bilayer IO films exhibit good electrochromic properties which is promising for applications in electrochromic smart windows.

References

- (1) E. Armstrong, D. McNulty, H. Geaney, and C. O'Dwyer, *ACS Appl. Mater. Interfaces*, **7**, 27006 (2015).
- (2) W. Zhou, L. Lin, W. Wang, L. Zhang, Q. Wu, J. Li, and L. Guo, *J. Phys. Chem. C*, **115**, 7126 (2011).
- (3) M. Zalfani, Z.-Y. Hu, W.-B. Yu, M. Mahdouani, R. Bourguiga, M. Wu, Y. Li, G. Van Tendeloo, Y. Djaoued, and B. L. Su, *Appl. Catal. B: Environmental*, **205**, 121 (2017).
- (4) H.-W. Zhang, G.-T. Duan, G.-Q. Liu, Y. Li, X.-X. Xu, Z.-F. Dai, J.-J. Wang, and W.-P. Cai, *Nanoscale*, **5**, 2460 (2013).
- (5) H. Li, J. Theriault, B. Rousselle, B. Subramanian, J. Robichaud, and Y. Djaoued, *Chem. Commun.*, **50**, 2184 (2014).
- (6) L. I. Halaoui, N. M. Abrams, and T. E. Mallouk, *J. Phys. Chem. B*, **109**, 6334 (2005).
- (7) H. Yan, C. F. Blanford, B. T. Holland, W. H. Smyrl, and A. Stein, *Chem. Mater.*, **12**, 1134 (2000).
- (8) G. V. Freymann, V. Kitaev, B. V. Lotsch, and G. A. Ozin, *Chem. Soc. Rev.*, **42**, 2528 (2013).
- (9) B. Hatton, L. Mishchenko, S. Davis, K. H. Sandhage, and J. Aizenberg, *PNAS*, **107**, 10354 (2010).
- (10) J. E. G. J. Wijnhoven and W. L. Vos, *Science*, **281**, 802 (1998).
- (11) O. D. Velev and A. M. Lenhoff, *Curr. Opin. Colloid Interface Sci.*, **5**, 56 (2000).
- (12) F. Pan, J. Zhang, C. Cai, and T. Wang, *Langmuir*, **2**, 7101 (2006).
- (13) F. Marlow, P. Sharifi, and R. Brinkmann, *Angew. Chem. Int. Ed.*, **48**, 6212 (2009).
- (14) J. Li, Y. Qin, C. Jin, Y. Li, D. Shi, L. Schmidt-Mende, L. Gan, and J. Yang, *Nanoscale*, **5**, 5009 (2013).
- (15) C. Li, G. Hong, and L. Qi, *Chem. Mater.*, **22**, 476 (2010).
- (16) Y. Xu, X. Zhu, Y. Dan, J. H. Moon, V. W. Chen, A. T. Johnson, J. W. Perry, and S. Yang, *Chem. Mater.*, **20**, 1816 (2008).
- (17) H. Ichinose, M. Terasaki, and H. Katsuki, *J. Sol-Gel Sci. Technol.*, **22**, 33 (2001).
- (18) L. Ge, M. X. Xu, and M. Sun, *Mater. Lett.*, **60**, 287 (2006).
- (19) T. Ohsaka, F. Izumi, and Y. Fujiki, *J. Raman Spectrosc.*, **7**, 321 (1978).
- (20) S. Balaji, Y. Djaoued, and J. Robichaud, *J. Raman Spectrosc.*, **37**, 1416 (2006).

Publisher's Note Springer Nature remains neutral with regard to jurisdictional claims in published maps and institutional affiliations.